Full-field hygroscopic characterization of paper inter-fiber bonds and the implications on network hygro-expansivity

Cellulose (2024) 31:567–586
https://doi.org/10.1007/s10570-023-05614-w

ORIGINAL RESEARCH

Full-field hygroscopic characterization of paper inter-fiber bonds and the implications on network hygro-expansivity

Niels Vonk · Ron Peerlings · Marc Geers · Johan Hoefnagels

Received: 29 March 2023 / Accepted: 10 November 2023 / Published online: 29 November 2023

Abstract The state-of-the-art in paper micro-mechanics calls for novel experimental data covering the full-field hygro-expansion of inter-fiber bonds, i.e., the 3D morphological changes and inter-fiber interactions. Therefore, a recently developed full-field single fiber hygro-expansion measurement methodology based on global digital height correlation is extended to orthogonal inter-fiber bonds, to investigate their full-field quasi-3D hygroscopic behavior. A sample holder has been developed which enables the quasi-3D characterization of the initial geometry of individual inter-fiber bonds, including the fiber thickness and width along the length of the fibers as well as the degree of wrap around and contact area of the bond, which are vital for understanding the inter-fiber bond hygro-mechanics. Full-field hygroscopic testing reveals the inter-fiber interactions: (i) the transverse hygro-expansion of each fiber strongly reduces when approaching the bonded area, due to the significantly lower longitudinal hygro-expansion of the other bonded fiber. (ii) The relatively large transverse strain of one fiber stretches the other crossing fiber in its longitudinal direction, thereby significantly contributing to the sheet scale hygro-expansion. (iii) Out-of-plane bending is observed in the bonded region which is driven by the significant difference in transverse and longitudinal hygro-expansion of, respectively, the top and bottom fiber constituting the bond. A bi-layer laminate model is employed to rationalize the bending deformation and an adequate match is found with the experimental data. Under the assumption of zero bending, which represents constrained inter-fiber bonds inside a paper sheet, the model can predict the contribution of the transverse strain in the bonded regions to the sheet-scale hygro-expansion.

Keywords Full-field measurement · Global digital height correlation · Hygro-expansion · Inter-fiber bond · Paper fibers

Introduction

The moisture-induced dimensional changes, i.e. the hygro-expansion, of paper-based products have been studied extensively over the past decades, but still leave many open questions for many applications (Alava and Niskanen 2006; Fellers 2007). For instance, better understanding of the hygro-expansion of paper is essential for printing applications to minimize detrimental macroscopic out-of-plane deformations of the paper sheet known as fluting, cockling, and curling (Kulachenko et al. 2005; Bosco et al.

Supplementary Information The online version contains supplementary material available at https://doi.org/10.1007/s10570-023-05614-w.

N. Vonk · R. Peerlings · M. Geers · J. Hoefnagels (✉)
Department of Mechanical Engineering, Eindhoven University of Technology, Eindhoven, The Netherlands
e-mail: J.P.M.Hoefnagels@tue.nl

2018; Kulachenko 2021). These phenomena are governed by a cascade of complex mechanisms occurring at all relevant underlying length scales, i.e. at the scale of single fibers, inter-fiber bonds, and fiber networks.

Because testing the microscopic paper components is challenging, most literature focuses on in-plane sheet-scale hygro-expansion measurements, complemented by inter-fiber bond models to explain the findings, see, e.g., Fellers (2007), Uesaka and Qi (1994), Niskanen et al. (1997) and Larsson and Wågberg (2008). These sheet-scale hygro-expansion tests typically involve measuring the sample dimensions as a function of the relative humidity (RH) (Fellers 2007). The micro-scale natural fibers are the main constituent of the paper sheet, and their hygro-expansion, which is significantly larger (20–40 times) in transverse compared to longitudinal direction (Fellers 2007; Vonk et al. 2021), drives the hygro-expansion of the paper sheet (Page and Tydeman 1962). Back in 1994, Uesaka (1994) stated that, for machine paper [with a fiber orientation distribution which is strongly aligned with the machine direction (MD)], the longitudinal hygro-expansion of the fibers is comparable to the sheet-scale hygro-expansion in MD, indicating that the longitudinal fiber hygro-expansion governs the sheet scale expansion in MD. In contrast, for non-oriented handsheets, yielding isotropic sheet-scale hygro-expansion, the longitudinal hygro-expansion of the fibers mainly contributes in the freestanding segments, whereas the significantly larger transverse hygro-expansion is transferred in the bonded regions in order to contribute to the sheet scale expansion (Wahlström 2009; Berglund 2011). This bond strain transferal was experimentally studied first by Page et al. (1962) and later by Nanko and Wu (1995). The authors demonstrated experimental evidence of the transferal of the relatively larger transverse strain of one fiber to another fiber in the bonded regions (referred to as transverse strain transferal). However, the results were not entirely conclusive regarding quantification of the transverse strain transferal, which was roughly estimated to be up to 50%.

A modeling approach also allows describing the inter-fiber bonds and investigating the transverse strain transferal. To this end, multiple fiber network models describing the moisture-induced deformations have been proposed over the years, e.g., idealized network models (Bosco et al. 2015a, b), random network models (Strömbro and Gudmundson 2008; Bosco et al. 2016, 2017; Samantray et al. 2020), and 3D beam network models (Sellén and Isaksson 2014; Motamedian and Kulachenko 2019; Brandberg et al. 2020). For instance Brandberg et al. (2020) proposed a 3D beam network model to distinguish the contribution of the longitudinal and transverse fiber hygro-expansion coefficient to the sheet-scale hygro-expansion. It was demonstrated that the longitudinal hygro-expansion coefficient (chosen as $\beta_l = 0.03$) of the fibers was directly taken up by the network, whereas only $\sim 4\%$ of the transverse hygro-expansion coefficient ($\beta_t = 0.6$) was transferred, resulting in an isotropic sheet-scale hygro-expansion coefficient of $(\beta_l + 0.04\beta_t \approx)0.054$, directly emphasizing the relatively weak contribution of the large transverse fiber hygro-expansion to the network. However, while all these models have their own merits, they require experimental identification and validation, in particular for the most significant and difficult aspect to characterize, the hygro-expansion behavior of inter-fiber bonded regions.

While the bond strength of isolated inter-fiber bonds, i.e., mode 1 and 2 fracture (Stratton and Colson 1990; Schmied et al. 2012; Fischer et al. 2012; Schmied et al. 2013; Jajcinovic et al. 2016, 2018), inter-fiber bond formation mechanisms (Nanko and Ohsawa 1989; Hirn and Schennach 2015), fiber-to-fiber contact surface measurements (Gilli et al. 2009; Kappel et al. 2009, 2010b, a), and complete 3D inter-fiber bond geometries including contact surface (Sormunen et al. 2019) have been characterized in great detail, direct data on the hygroscopic behavior of isolated inter-fiber bonds is lacking. As stated before, Page et al. (1962) were the first to analyze the transverse strain transferal, and stated that transverse shrinkage of a fiber causes increased longitudinal contraction of an (more or less) orthogonally bonded fiber, thus forming micro-compressions in the bonded region identified as wrinkles. However, the authors could not quantify the portion of transverse strain which was transferred to the other fiber. Nanko and Wu (1995) followed up on this work and studied the fiber shrinkage in freestanding and bonded segments during paper formation by determining the length difference between silver grains applied to (near orthogonally bonded) fiber networks in the wet (moisture content of 60%) and dry state (RH = 60%). The authors reported that upon drying the freestanding

fiber segments shrunk significantly less compared to the bonded segments, confirming the transverse strain transferal. Identification of the transverse shrinkage of the freestanding fiber segments in the wet webs enabled a quantitative comparison between the bond strains, from which the authors extracted a transverse strain transferal of up to 50%. This is much larger than the contribution of ~ 4% found in the 3D network model proposed by Brandberg et al. (2020). The large measurement uncertainty in the results of Nanko and Wu (1995) stems from the accuracy of the silver grain method in which relatively small strains are determined over short lengths (i.e., 30–100 µm), containing considerable topographical fluctuations. Moreover, the dry observations were only compared to the fully wet state, where the inter-fiber bonds are weak and not properly formed, entailing significant morphological changes at the bonding surface with fiber-to-fiber in-plane rotations. In contrast, the geometry is relatively "fixed" during hygro-expansion simulations with the 3D network model. Furthermore, Nanko and Wu (1995) characterized the inter-fiber bonds inside the paper sheet, where each bond is influenced by its neighboring fibers, making it difficult to unravel the individual contributions to the network.

Because the work of Nanko and Wu (1995) showed such intriguing and important results for the paper community, in this work we aim to exploit the advances in microscopy and image correlation techniques over the past decades, to devise a new methodology to quantitatively characterize the full-field 3D hygro-expansion of isolated inter-fiber bonds during the full wetting and drying cycle. This results in full-field strain maps in and around the bonded area, enabling the validation of the above-described network models. The recently developed full-field methodology based on Global Digital Height Correlation (GDHC), that enables the characterization of the single fiber hygro-expansion with great precision and robustness, is instrumental in reaching this goal (Vonk et al. 2020). By extending this methodology towards single (isolated) inter-fiber bonds, it should be possible to measure the full-field hygro-expansion, including the variation of the strain field around the bonded area, transverse strain transfer in the bonded region, and comparison of freestanding to bonded segment characteristics during wetting and drying.

To achieve this goal, the following key challenges need to be overcome: (i) isolation, clamping and preparation of inter-fiber bonds, which poses a challenge compared to single fibers, (ii) in order to understand the mechanics of the inter-fiber bonds, the initial 3D geometry is required, i.e., thickness of the bonded fibers, degree of wrap around, and an estimation of the bonded area, and (iii) the kinematic regularization used to describe the displacement fields in the GDHC algorithm must be improved, as significantly larger strain gradients are expected than for single fibers. To address challenges (i) and (ii), a custom sample holder has been designed that allows for double sided imaging of isolated orthogonal inter-fiber bonds to obtain a quasi-3D high-resolution reconstruction of the initial geometry. Challenge (iii) is addressed by performing a polynomial order variation to find the correct strain fields (Vonk et al. 2020; Neggers et al. 2014; Hoefnagels et al. 2022). It will be shown that this methodology enables the identification of the full-field 3D hygro-expansion of inter-fiber bonds and their mechanics, covering (i) accurate longitudinal and transverse strain gradients around the bonded area and (ii) the magnitude of the transverse strain transferal from fiber-to-fiber in the bonded region. Moreover, a bi-layer laminate model of the bonded area will be proposed to describe the inter-fiber bond mechanics, which is used to validate and improve the (commonly adopted) fiber stiffness parameters used in previous inter-fiber bond models (Brandberg et al. 2020; Magnusson and Östlund 2013). The model also allows to rationalize and predict the transverse strain transferal inside the paper sheet.

Materials and methods

Preparation of inter-fiber bonds and single fibers

Isolated inter-fiber bonds are formed from softwood pulp following the same method as proposed by Forsström et al. (2005) and Kappel et al. (2009). The preparation involves applying small droplets of highly diluted pulp in between two Teflon (PTFE) sheets which is subsequently dried using a conventional sheet dryer. Sparse networks of fibers are subsequently obtained, from which single fibers or inter-fiber bonds can be cut. A nominal pressure (20 kPa) is applied, however, the local pressure applied to the fibers and fiber joints in the sparse web, initiating inter-fiber bond formation, is significantly higher.

Since the paper sheet hygro-expansivity depends on the amount of stress applied during drying (Lindner 2018), the differences in local pressure applied to the fiber joints in the sparse networks may lead to a systematic offset in the hygro-expansivity of the fibers. In order to properly interpret the inter-fiber bond hygro-expansion results, it is essential to know the scatter in fiber hygro-expansion prior to investigating the fiber-to-fiber (hygro-expansion) interactions. Hence, the hygro-expansion of single fibers isolated from the created sparse networks are tested first. Note that the pulp consists of the same mixture of spruce and pine as studied in Vonk et al. (2021).

Single fiber hygro-expansion measurement methodology

Single fibers are isolated from the pressed sparse networks by means of cutting and subsequently clamped onto a glass slide using two highly compliant 50 µm thick nylon wires, following the methodology proposed in Vonk et al. (2020). To enable Global Digital Height Correlation (GDHC), a random pattern of 500 nm polystyrene particles is applied to the fibers using a dedicated mystification setup (Shafqat and Hoefnagels 2021). The prepared fibers are tested individually inside a climate chamber underneath an optical profilometer, in which the RH around the fiber is controlled and cyclically varied from 30 to 90% RH, while consecutive topographies of the fiber top surface are captured to measure the 3D deformation over time. After testing, the obtained topographies are processed using the GDHC algorithm to extract the displacement fields U_x, U_y and U_z. The GDHC algorithm uses so-called shape functions, in this case 3D spatial polynomial functions, to map the deformed configuration back to the initial configuration. The optimal amplitudes of these shape functions are found using an iterative modified Newton–Raphson scheme in which the so-called "correlation residual", i.e. the difference between the initial and the back-deformed configuration, is minimized (Neggers et al. 2016). By finding the minimal correlation residual, the 3D displacement fields are obtained, which are combined with the initial fiber topography data to enable quantification of the full-field quasi-3D hygro-expansion, i.e. the longitudinal (ϵ_{ll}), transverse (ϵ_{tt}) and shear (ϵ_{lt}) components of the surface strains, i.e. strains that are computed along the curved fiber surface (Shafqat et al. 2018). More details on the testing methodology and GDHC algorithm can be found in Neggers et al. (2014, 2016) and Vonk et al. (2020).

Three fibers are subjected to four RH cycles, each varying from 30–90–30%, as given in Fig. 1. A linear slope of 0.5%/min is used to change the RH set-point, which is kept constant for 2 h to study possible creep effects at high and low RH levels, similarly to the experiments conducted in Vonk et al. (2021). Regarding acquisition, a magnification 55× (100× objective with 0.55× field-of-view (FOV) multiplier) was used, reducing the FOV to 147×111 µm^2 (1400×1040 pixels), which is adequate to capture the nano-particles with sufficient detail and visualize enough fiber surface.

Single fiber hygro-expansivity

The hygroscopic responses of the tested fibers are shown in Fig. 1. The fiber-to-fiber scatter of the transverse (and longitudinal) hygro-expansivity is remarkably large, i.e. an average strain difference of ~ 1.5% for fiber 1 to ~ 5% for fiber 3 is found. Vonk et al. (2021), it was demonstrated that the transverse hygro-expansion of the five softwood fibers (of the same pulp) picked directly from the pulp bale was 5.8 ± 0.6%, demonstrating a significantly lower scatter. Furthermore, the ongoing transverse shrinkage suggests that the three fibers in Fig. 1 were subjected to a large drying stress, imposing an irreversible initial strain after drying, known as dried-in strain, which is released during the subsequent wetting and drying cycles. Fiber 3 shows a larger hygro-expansion than fiber 1 for the same RH change, which may be attributed to the amount of (positive) dried-in-strain stored in the fiber structure. It is most likely that the fiber with the highest hygro-expansivity was subjected to the lowest drying stress, because a stress-free fiber has more freedom to swell compared to a fiber subjected to a larger dried-in strain.

These experiments demonstrate that a large scatter in hygro-expansivity is found for fibers which are prepared following the inter-fiber bond methodology proposed by Forsström et al. (2005) and Kappel et al. (2009). Hence, it may be expected that this scatter in hygro-expansion will also be present in the fibers which are part of the inter-fiber bonds.

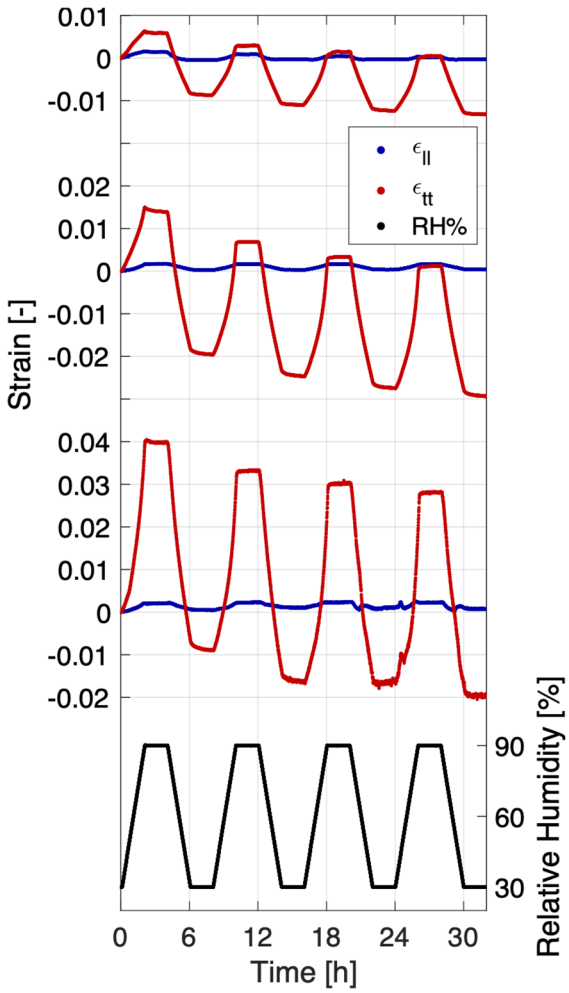

Fig. 1 Hygroscopic response of single fibers prepared according to the methodology proposed by Forsström et al. (2005) and Kappel et al. (2009) subjected to four cycles, each ranging from 30 to 90% RH. The responses show a large fiber-to-fiber scatter in hygro-expansion which is attributed different degrees of restraint acting on the fiber during drying. The gradual overall shrinkage of the fibers is driven by the release of the dried-in strain stored inside the fibers due to this restraint

Extension of the methodology to inter-fiber bonds

Initial inter-fiber bond characterization

The full-field single fiber hygro-expansion methodology is naturally extended to (isolated) inter-fiber bonds. Orthogonal inter-fiber bonds are cut from the prepared sparse networks and clamped onto a specifically designed sample holder using two 50 µm nylon wires to minimize rigid body translations and to keep the inter-fiber bond inside the FOV of the microscope, whereby the wires still allow for fiber swelling and (reduced) rotation and bending, see Fig. 2a. As the hygro-mechanics of inter-fiber bonds is more difficult to interpret than that of single fibers, it is necessary to know the initial 3D geometry of each tested inter-fiber bond, i.e., the thickness and width of the fibers along their length, as well as the wrap around angle, contact surface and fiber-to-fiber bond angle. Furthermore, the initial 3D geometry is also required for the bi-layer laminate model describing the mechanics of the bonded area, see Section "Bi-layer laminate model describing the bonded area" below. To enable the measurement of the 3D geometry of the inter-fiber bonds, the specifically designed sample holder schematically shown in Fig. 2a is used, consisting of two thin (~ 100 µm) glass slides, spaced ~ 300 µm from each other, glued to a PMMA frame.

Placing a mirror (e.g. silicon wafer) underneath the prepared specimen allows to visualize two aligned topographies of the front and back of the inter-fiber bond as proposed by Maraghechi et al. (2023) and shown in Fig. 2b. The quality of the back topography is significantly less than that of the front due to the loss of brightness caused by the light rays being blocked by the inter-fiber bond, when the image is made via the mirror. The offset between the two topographies is known from the piezo-actuator inside the optical profilometer with reasonable accuracy (~ 1 µm, determined by measuring wires of known diameter), allowing to convert the two topographies into a fiber thickness map as shown in Fig. 2c. Computing the fiber width average height profile, shown in Fig. 2d, allows for determining the degree of wrap around, given as $\phi_{-,1}$ and $\phi_{-,2}$ for, respectively, both sides of the bottom fiber, and $\phi_{+,1}$ and $\phi_{+,2}$ for the top fiber. The top and bottom fiber are labeled with, respectively, + or − in the following. Furthermore, the contact surface area is estimated using the methodology proposed by Kappel et al. (2009), where the dark areas in the polarization optical microscopy images, shown in Fig. 2d, indicate the bonded regions. Finally, the fiber-to-fiber bond angle, given by α in Fig. 2b is also determined. In this work a total of four inter-fiber bonds are characterized and tested, and Table 1 shows the obtained characteristics for every inter-fiber bond, i.e. fiber thickness (t), and

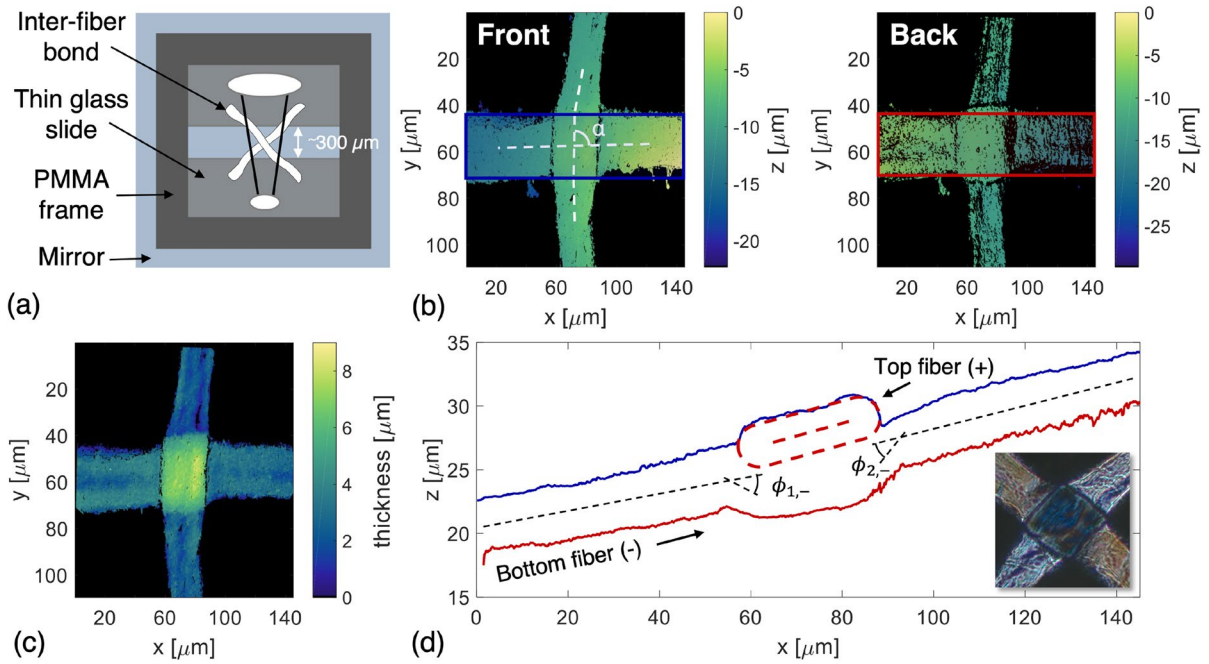

Fig. 2 Initial characterization of an inter-fiber bond: **a** schematic of the sample holder which allows double sided imaging of the inter-fiber bond (Maraghechi et al. 2023), **b** front and back topography of an inter-fiber bond with fiber-to-fiber bond angle α, **c** thickness map, and **d** fiber width averaged height profile of the front and back of the bottom (horizontal) fiber which allows determination of the interface angle $\phi_{1,-}$ and $\phi_{2,-}$ for the bottom fiber and polarization optical microscopy image of the bonded region, in which the dark areas indicate bonding. In the following, the top and bottom fiber are labeled as, respectively, + and −

width (w), wrap around angle (ϕ), estimated contact surface (A) with bonded fraction, and fiber-to-fiber bond angle (α). Please note that two inter-fiber bonds reveal a bond angle of 90°, whereas the two other bonds have a smaller angle, respectively, 71 and 78°.

Acquisition and GDHC parameter determination

After the initial characterization, the specimen is patterned and tested following the single fiber procedure described in Section "Single fiber hygro-expansion measurement methodology" and Vonk et al. (2020). Each inter-fiber bond is subjected to a RH cycle of 30–90–30% for four cycles, with a constant rate of 0.1%/min and a plateau of 5 h at 90 or 30%, resulting in a total time per inter-fiber bond of 120 h. The small rate is necessary to be able to capture seven parallel 55× topographies (with a FOV of 147 × 111 μm^2) of the inter-fiber bond with its four connected "arms" with sufficient detail for the GDHC. Please note that the inter-fiber bond 2 is imaged using a magnification of 100× (FOV of 81 × 61 μm^2) because the width of

Table 1 Inter-fiber bond characteristics: fiber thickness (t), fiber width (w), interface angle ($\phi_{1,2}$) of the top (+) and bottom (−) fiber, contact surface (A), and bond angle (α)

inter-fiber bond	t_+ (μm)	t_- (μ)	w_+ (μm)	w_- (μm)	$\phi_{1,+}$, $\phi_{2,+}$ (°)	$\phi_{1,-}$, $\phi_{2,-}$ (°)	A (μm^2)	α (°)
1	2.8	3.2	57	53	2.6, 6.4	4.2, 6.5	2533 (84%)	90
2	3.2	4.1	25	28	11.0, 8.7	11.2, 14.4	623 (89%)	90
3	1.5	4.2	44	62	1.5, 2.4	2.6, 5.8	1140 (76%)	79
4	1.5	5.1	61	64	1.7, 0.9	3.1, 3.8	3475(89%)	78

both fibers is significantly smaller than in the other inter-fiber bonds, see Table 1. As an example, the location of the seven topographies (topo) are shown in Fig. 3. An overlap of 25% of the height and width of the topographies is chosen.

Two different correlation strategies can be used to obtain the full-field behavior of the tested inter-fiber bonds: correlating the stitched images and extracting continuous deformation fields, or correlating the seven images separately, resulting in dis-continuous deformation fields. Prior analysis revealed that the stitched images cannot trivially be used in the GDHC algorithm to obtain a continuous strain field, as the stitching introduces sub-pixel artifacts into the images which would result in artificial strain spots. Nevertheless, a high strain precision along the full inter-fiber bond surface is required since longitudinal strains of around 0.2% are expected (Vonk et al. 2021). To achieve sufficiently precise strains, each of the topographies is correlated individually in each of the eight regions-of-interest (ROIs), after which the resulting individual strain fields are stitched into continuous strain profiles. To this end, ROIs 1–3a–5 are combined for the top fiber strain profiles and ROIs 6, 3b and 7 for the bottom fiber strain profile.

Vonk et al. (2020), it was found that a second order polynomial in both fiber length and width direction offered the best kinematic regularization for describing single fiber swelling. However, as significantly larger strain gradients are expected in and around the bonded area, a higher order polynomial description is required to properly describe the displacement fields at and near the bonded area. Therefore, a polynomial order analysis, as done by Neggers et al. (2014) and Hoefnagels et al. (2022), is conducted. The strain gradients in the transverse direction of the fiber are expected to be similar to single fibers, whereas major variations are expected along the longitudinal direction. Hence, the eight ROIs are correlated using a 2nd–5th order polynomial description in the transverse and 2nd–7th order in the longitudinal direction. The correlation residual and strain fields for every polynomial combination are assessed and it is found that for ROI 1 and 5 a second order polynomial field in both direction suffices. For ROI 2, 4, 6, and 7 (closer to the bonded area) a third order polynomial and second order in, respectively, longitudinal and transverse direction appears to be optimal. ROI 3a, containing the top fiber, requires a fourth order

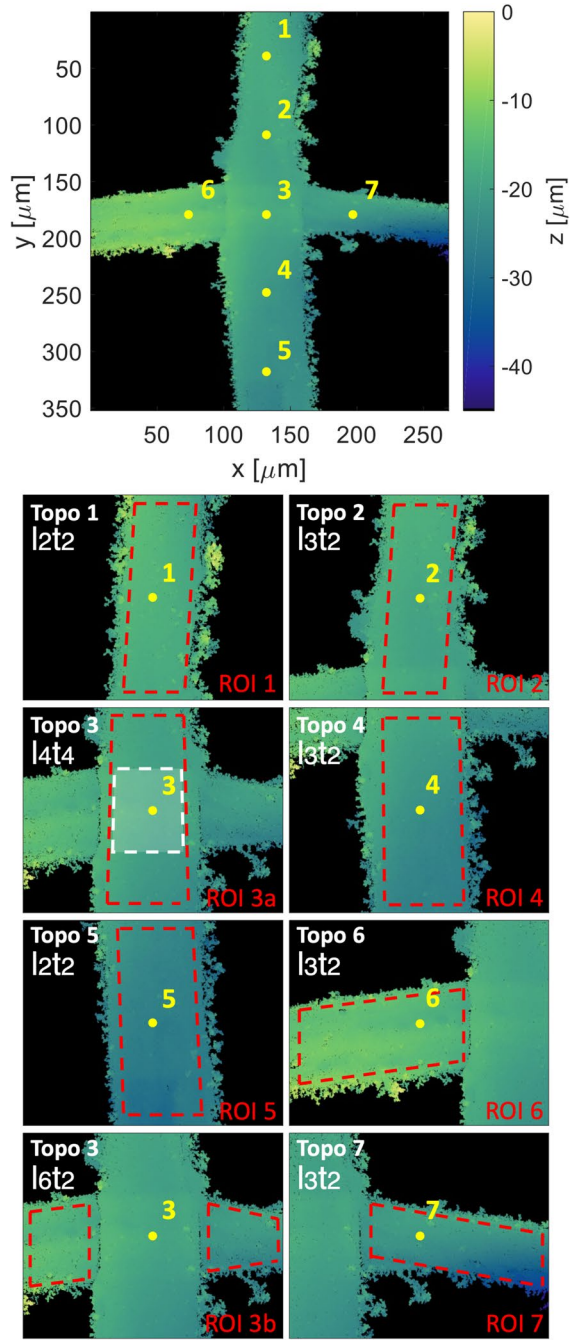

Fig. 3 Stitched image of an inter-fiber bond with the location of the centers of the seven separate topographies depicted below. The seven ROIs used in the GDHC are highlighted in the separate images and the optimal order of the polynomial field is added, where, e.g., "l3t2" indicates that a third and second order polynomial is used in, respectively, the longitudinal and transverse direction for the correlation. Please note that image 3 is correlated twice, with different ROIs, since it contains both the bottom and top fiber. The central area of ROI 3a is highlighted in white which indicates the bonded area used in Fig. 6 below

polynomial in both directions, while the bottom fiber in ROI 3b, is best correlated using a sixth and second order polynomial in, respectively, longitudinal and transverse direction. The polynomial orders used for the correlation of each ROI are added to Fig. 3, where, for instance, the code "l3t2" indicates a third and second order polynomial in, respectively, longitudinal and transverse direction. ROI 3b consists of two separate ROIs that are correlated at once with a continuous "l6t2" displacement field, thereby taking into account the relative displacement between the fiber segments left and right of the bonded area. The resulting displacement field provides, by means of interpolation, an estimate of the longitudinal (horizontal) strain field inside the bonded area at the fiber-to-fiber interface surface, as detailed below.

Data processing

The longitudinal and transverse hygro-expansion, averaged over the fiber width, for an RH increase of 30–90% (cycle 2) of the top and bottom fiber for each ROI is given in Fig. 4a. The trends in the curves are clear, but quantitative mismatches emerge in the overlap regions. This is driven by the fact that polynomials (especially higher order) tend to fluctuate near the edges of the ROI (Neggers et al. 2014).

To remedy this issue, in the overlap area, the strain values are stitched by linearly scaling the strains of one of the two adjacent ROIs from 1 to 0, while in the adjacent ROI a reverse scaling from 0 to 1 is used, and adding both scaled strains, in the spirit of a partition of unity, to yield the stitched strains. Additionally, an error for every average strain point is determined to estimate the stitching error. However, the outer edges of e.g. ROI 3b in Fig. 4a reveal such large non-physical deviations, i.e. these faulty regions are not adequately reduced by the linear scaling, that they need to be discarded. Hence, a factor Δ is introduced, representing a band at the left and/or right side of each ROI in the overlap region which will not be taken into account in combining the strain curves. E.g., for a factor Δ of 0.1, the combined strain response in the overlap area from left to right in Fig. 4 is built of (i) the strain curve of the left ROI in the first 10%, (ii) the combined strain response of both ROIs in the following 80%, and (iii) the strain curve in the right ROI in the final 10%. For a factor Δ of 0.2, this changes to 20% of the left ROI, 60% combined, and 20% right.

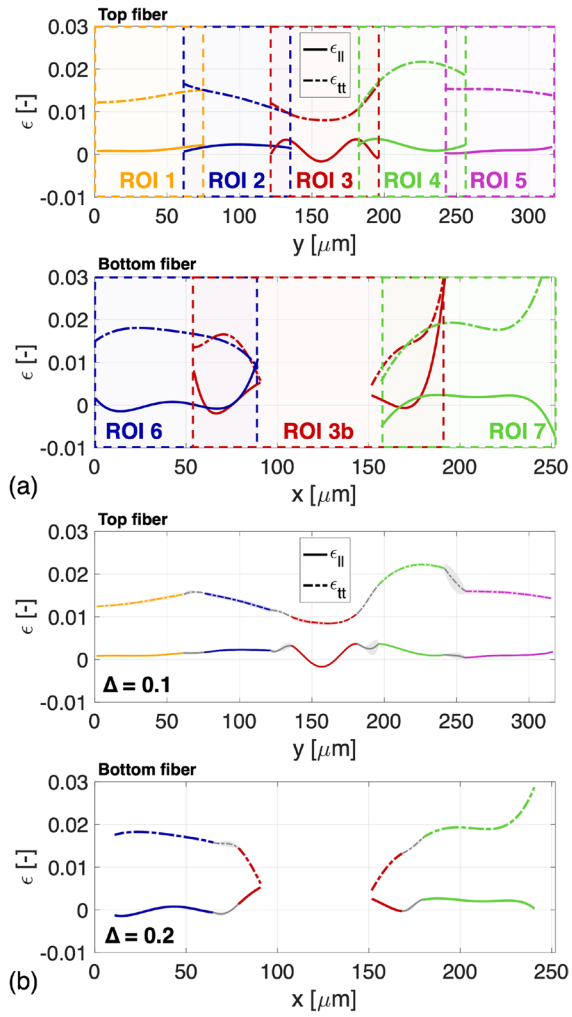

Fig. 4 The fiber width averaged transverse and longitudinal strain increase from 30 to 90% RH of the top and bottom fiber for each correlated ROI, with **a** the unprocessed strain trend of each ROI correlation, showing clear mismatches in the overlap regions, and **b** continuous strain curves, with reduced errors in the overlap regions, by means of linear scaling, for two different values of the width Δ of a band of data points spanning the edge of the overlap region. A factor Δ of 0.1 represents a band of 10% of the overlap region which is neglected in the average trend determination in the overlap regions

By neglecting these boundary regions the expected accuracy of the measurement is further improved. After comprehensive analysis, a Δ of 0.1 and 0.2 provides the best results for, respectively the top and bottom fiber for all tested inter-fiber bonds, and the resulting strains are plotted in Fig. 4b. The larger factor Δ for the bottom fiber is attributed to ROI 3b

being correlated with a higher order polynomial field compared to the top fiber, hence the errors around the edges of ROI 3b span a wider region. In the resulting stitched strain profiles, no discontinuities can be spotted (see, e.g., Fig. 4b) and a smooth curve is obtained for all strain profiles of all inter-fiber bonds. Please note that, while the overlap region of the topographies for every inter-fiber bond and Δ are equal for every inter-fiber bond, the size of the overlap regions in the strain curves differ somewhat because the bounds of the correlated ROIs are not the same.

Results and discussion

Full-field hygro-expansivity

To explore the full-field nature of the resulting data, as given for inter-fiber bond 1 in Fig. 4b, the fiber-width averaged longitudinal and transverse strain of, respectively, the top and bottom face along the fiber lengths for an RH increase from 30 to 90% of all inter-fiber bonds are determined. The horizontal and vertical strain curves of all inter-fiber bonds are presented in Fig. 5, where the transverse strain of the top fiber ($\epsilon_{tt,+}$) and the longitudinal strain of the bottom fiber ($\epsilon_{ll,-}$) are oriented in the horizontal direction, whereas the longitudinal strain of the top fiber ($\epsilon_{ll,+}$) and the transverse strain of the bottom fiber ($\epsilon_{tt,-}$) are both oriented in the vertical direction, both at different heights through the thickness of the inter-fiber bond. Note that the centers of the bonded area of the top and bottom fiber are centrally aligned, and the strain along the global fiber axes are plotted for the non-orthogonal bonds. The average strain profiles, based on wetting cycles 2–4 (because the first wetting cycle shows a significant release of dried-in strain as shown in Fig. 6a below), is shown together with its standard deviation, that is visualized by the (often very thin) band around the curves.

First, the hygroscopic behavior of each RH cycle is reproducible, because the resulting scatter for each strain component is low, highlighting the accuracy of the used GDHC method. Furthermore, when considering the strains in the bonded region, a repeating pattern is visible for every inter-fiber bond: (i) the transverse strain of both fibers ($\epsilon_{tt,+}$ and $\epsilon_{tt,-}$) decreases when approaching the bonded area, which is attributed to the low longitudinal strain of the bonded fiber, combined with a larger longitudinal stiffness (Magnusson and Östlund 2013; Czibula et al. 2021), constraining the transverse hygro-expansion, (ii) the longitudinal strain of the top fiber shows compression in the bonded area, which is due to the out-of-plane bending of the bond, as studied numerically by Brandberg et al. (2020) and analyzed in more detail below, and (iii) the longitudinal strain of the bottom fiber ($\epsilon_{ll,-}$), with the interpolated strain field depicted by the dashed line, increases when approaching the bonded area from both sides. This suggests that the large transverse strain of the top fiber stretches the bottom fiber in its longitudinal direction, as observed earlier by Nanko and Wu (1995).

These observations are strong evidence that the hygro-mechanical behavior of the isolated inter-fiber bonds is qualitatively consistent (and the measurement method reproducible) even for inter-fiber bonds consisting of deviating fiber geometries and fiber-to-fiber bond angles (as seen for inter-fiber bonds 3 and 4). Note that for inter-fiber bond 3, five and three topographies have been used to image, respectively, the bottom and top fiber instead of vice versa (as done for the other inter-fiber bonds). This was necessary to accommodate the severe fiber surface roughness at the far ends of the vertical fiber.

The average strain in the bonded area (i.e. the average bond strain) is determined and depicted in each graph in Fig. 5 by $\epsilon^{BA}_{ll,+}$, $\epsilon^{BA}_{tt,+}$, $\epsilon^{BA}_{ll,-}$, and $\epsilon^{BA}_{tt,-}$. The magnitude of $\epsilon^{BA}_{ll,+}$, $\epsilon^{BA}_{tt,+}$, and $\epsilon^{BA}_{ll,-}$ is determined by considering the central area of the strain field in the bond, i.e. a band of 25% around the strain field is excluded, as depicted in Fig. 5. The transverse average bond strain of the bottom fiber ($\epsilon^{BA}_{tt,-}$) is determined as follows. Considering that the longitudinal strain of the top fiber constrains and reduces $\epsilon_{tt,-}$ at the bonded area, $\epsilon^{BA}_{tt,-}$ should be equal to or lower than the value of $\epsilon_{tt,-}$ just next to the bond. Hence, $\epsilon^{BA}_{tt,-}$ is taken as the average of the closest measurement value of $\epsilon_{tt,-}$ left and right of the bonded area. Note that each of the bond strain values, ϵ^{BA}, is taken as the average of cycles 2–4. In summary, the obtained full-field hygro-expansivity data allows for accurate longitudinal and transverse strains in and around the bonded region. Moreover, the full-field data enables identification of the average bond strains at the top fiber surface and the fiber-to-fiber interface in longitudinal and transverse direction.

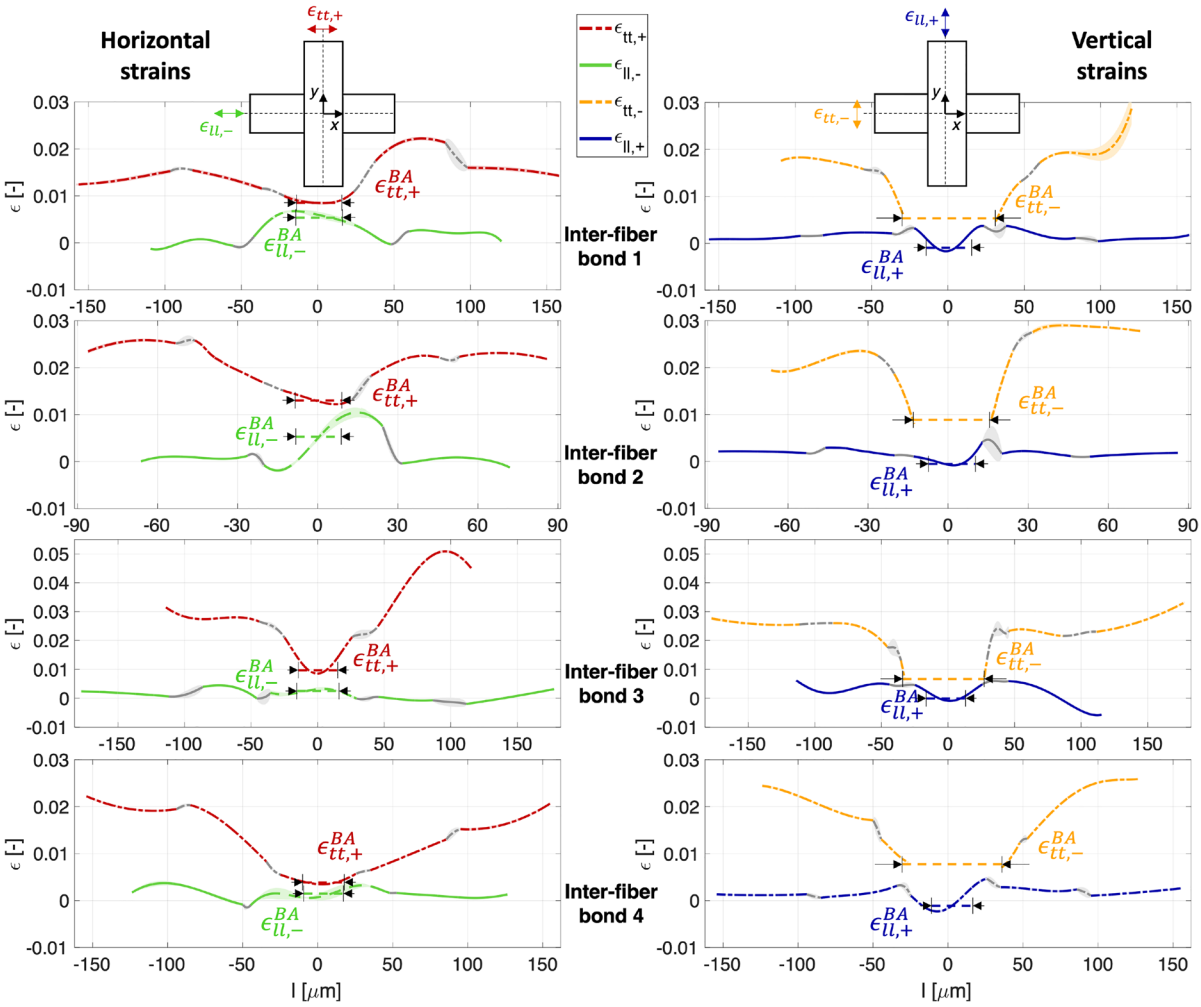

Fig. 5 Fiber-width averaged longitudinal and transverse strain of the top and bottom fiber along the fiber lengths for an RH increase of 30 to 90% of the inter-fiber bonds. The curves shown are the average curve of cycles 2–4 with its standard deviation shown by the shaded band which is often too thin to see. The transverse strain of the top fiber ($\epsilon_{tt,+}$) and the longitudinal strain of the bottom fiber ($\epsilon_{ll,-}$) are in the horizontal direction but at different heights of the bond, and the longitudinal strain of the top fiber ($\epsilon_{ll,+}$) and transverse strain of the bottom fiber ($\epsilon_{tt,-}$) are in the vertical direction. Similar responses are found for each inter-fiber bond, indicating qualitatively reproducible hygro-mechanical behavior. For each inter-fiber bond, (i) the transverse strain of the top and bottom fiber is smaller in and close to the bonded area, (ii) a smaller longitudinal strain of the top fiber ($\epsilon_{ll,+}$) and (iii) a larger longitudinal strain of the bottom fiber ($\epsilon_{ll,-}$) is found in the bonded region due to the transverse strain transferal of the top fiber. The average bond strain (ϵ^{BA}) is depicted in each graph by the horizontal dashed lines

In order to better understand the above-described strain curves, the inter-fiber bond hygro-mechanics need proper investigation as elaborated next.

Inter-fiber bond hygro-mechanics

Figure 6a shows the evolution of the field-averaged longitudinal and transverse hygro-expansion in the bonded region of ROI 3a (top fiber) of inter-fiber bond 1 (highlighted in white in Fig. 3), together with the RH that is controlled over time.

The overall transverse hygro-expansion response is similar to the single fiber responses displayed in Fig. 1, i.e. an overall release of irreversible (dried-in) strain. The transverse fiber hygro-expansion curve continuously drifts for multiple RH cycles,

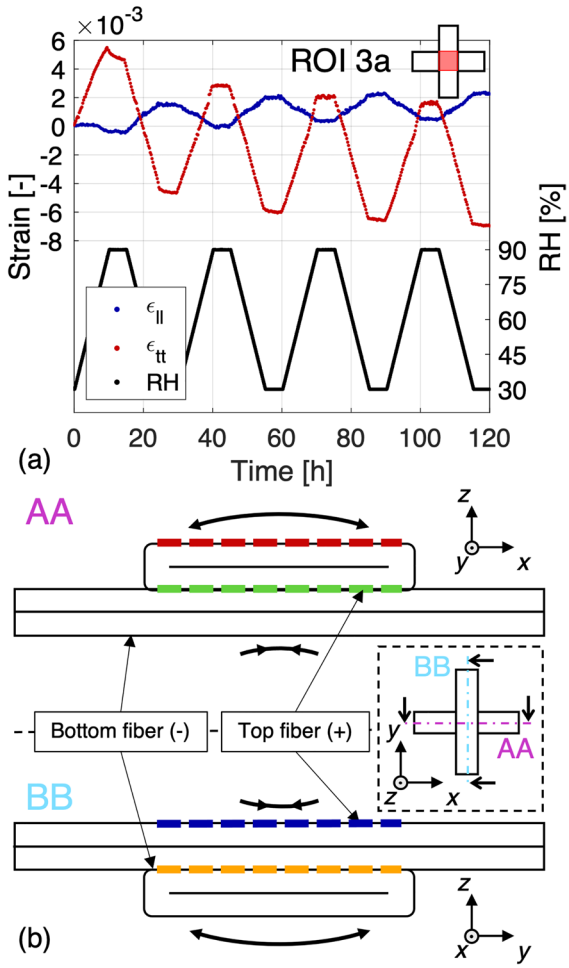

Fig. 6 Inter-fiber bond hygro-mechanics, with **a** the field-averaged longitudinal and transverse hygro-expansion in the bonded area of ROI 3a (highlighted white in Fig. 3), and the measurement of the RH, which is controlled over time, for inter-fiber bond 1. During the increase of RH, the increase of the transverse strain is accompanied by a decrease of the longitudinal strain, a phenomenon that is driven by the significantly larger transverse (compared to longitudinal) hygro-expansivity of the paper fibers, resulting in out-of-plane bending of the inter-fiber bond upon wetting or drying. In **b** cross-section AA shows downward bending because the top fiber expands more in its transverse direction than the bottom fiber in its longitudinal direction. Vice versa for cross-section BB, resulting in upward bending. The colors in the cross-sections correspond to the strain in longitudinal and transverse direction at, respectively, the top and interface surface, which are in the same direction for every cross-section

similar to Fig. 1. This is, however, inconsistent with restrained dried handsheets subjected to multiple RH cycles, of which the dried-in strain is fully released after the first RH cycle and the hygro-expansion curve, consequently, stabilizes. A possible theory might be that the fibers within the handsheets are far more constrained in contrast to the (almost) "unconstrained" inter-fiber bonds and fibers tested here, thereby disabling (full) release of dried-in strain during RH alternation. The (full) release of dried-in strain stored inside the "unconstrained" inter-fiber bonds and fibers tested here, apparently, occurs when subjected to multiple RH cycles. Note that this continuously drifting hygro-expansion curve was also observed for softwood and hardwood, pulp and paper fibers (Vonk et al. 2021, 2023a). The above theory is strengthened by the fact that restrained dried handsheets after the first RH cycle exhibit a (significantly) lower hygro-expansion than freely dried handsheets, indicating that dried-in strain remains stored inside the restrained dried handsheets after the first RH cycle. Furthermore, the transverse hygro-expansivity in Fig. 6a is significantly lower compared to the single fibers found in Fig. 1, implying a reduction of the transverse strain of the top fiber by the lower longitudinal strain of the bottom fiber, which are (globally) oriented in the same direction for inter-fiber bond 1 and 2 (with a bond angle of 90°). Moreover, for the wetting cycles 2–4, the longitudinal strain decreases for increasing RH, and vice versa, which contradicts the general explanation based on swelling or shrinkage during, respectively, moisture uptake or release. The only logical explanation for this negative longitudinal hygro-expansion at the top fiber surface in the bonded area during moisture uptake is upward (out-of-plane) bending, which is driven by the significant difference in longitudinal and transverse hygro-expansivity and stiffness of the fibers constituting the bond (Vonk et al. 2021; Magnusson and Östlund 2013), as also visualized by the 3D bond model proposed by Brandberg et al. (2020). Please note that all inter-fiber bonds reveal the same curve as given in Fig. 6a and hence display the described bending behavior, as visualized by the decrease in longitudinal strain for all inter-fiber bonds in Fig. 5)

Two schematic cross-sections of the inter-fiber bond are shown in Fig. 6b, where AA and BB

refer to, respectively, the horizontal and vertical cross-section. Cross-section BB is considered for understanding the behavior found in Fig. 6a. During moisture uptake, the bottom fiber swells significantly more in transverse direction than the top fiber in longitudinal direction, which causes upward bending. Reversely, in cross-section AA, the large transverse strain of the top fiber and small longitudinal strain of the bottom fiber results in downward bending. Note that the colors in the cross-sections are linked to the strains through the thickness of the bond, i.e. blue and red corresponds to, respectively the longitudinal and transverse strain at the top surface of the top fiber and green and orange to, respectively, the longitudinal and transverse strain of the bottom fiber at the interface surface, which are both in the same direction for the separate cross-sections.

It is unlikely that this out-of-plane bending also occurs for inter-fiber bonds located inside a paper sheet, where they are severely constrained by other fibers. Therefore, an analytical bending model for a inter-fiber bond based on classical laminate theory is proposed to rationalize this bending behavior. The model can subsequently be compared to the experimentally obtained average bond strains. If this model adequately captures the bond mechanics, it would allow to extrapolate the strain profile through the complete thickness of the inter-fiber bond, even at the bottom, which was not characterized. Additionally, the model (with different boundary conditions) may also be used for the inter-fiber bond hygro-mechanics inside a paper sheet, where minimal (or zero) bending is possible, thereby analyzing the transverse strain transferal at the sheet level. This bi-layer laminate model is explored next.

Bi-layer laminate model describing the bonded area

Because the width of the fibers is significantly larger than their thickness, classical laminate theory can be adopted to describe the bending deformation in the bonded area (Pister and Dong 1959; Reissner and Stavsky 1961). The laminate has two layers which represent one of the fibers in the bond each. Both layers are assumed to be transeversly isotropic with the isotropic axis coinciding with the fiber axis. They are rotated under an angle α with respect to each other in the plane of the plate/bond, as given in Table 1. α is 90° for inter-fiber bond 1 and 2, therefore, a perpendicular fiber bond geometry will be assumed in the model for now. Moreover, the strain through the thickness of the laminate ($\epsilon(z)$), is composed of an elastic strain (ϵ^E) and hygroscopic strain (ϵ^H),

$$\epsilon(z) = \epsilon^E(z) + \epsilon^H(z), \tag{1}$$

Assuming a linear dependency of the strain through the thickness corresponding to the curvature (κ) of the laminate results in

$$\epsilon(z) = \epsilon_0 - \kappa z, \tag{2}$$

in which ϵ_0 represents the strain value at the interface between the two fibers (defined as $z = 0$). Combining Eqs. (1) and (2), the following expression for the elastic strain is found:

$$\epsilon^E(z) = \epsilon_0 - \kappa z - \epsilon^H(z), \tag{3}$$

The hygroscopic strain (ϵ^H) is the piece wise constant and can be obtained from the measurements of the freestanding segments of the fibers at the outer ends, denoted as ϵ^f. The elastic strain (ϵ^E), and stress distribution associated with it governs the mutual restraint between the fibers. The strain at the interface (ϵ_0) and curvature of the laminate (κ) are yet to be determined in order to obtain the strain profile through the thickness of the bonded area.

Figure 7a displays two schematic cross-sectional representations of the bending problem in horizontal (AA) and vertical direction (BB). In cross-section BB, the longitudinal direction of the top fiber and the transverse direction of the bottom fiber are in y-direction (resulting in upward bending because the transverse hygro-expansivity is always larger than the longitudinal expansivity), and vice versa in x-direction for cross-section AA (resulting in downward bending). Note that perfect bonding between the two fibers is assumed in this model.

The goal is to determine ϵ_0 and κ (Eq. 2) in xx-, yy- and xy-direction, i.e. $\epsilon_{0,yy}$, $\epsilon_{0,xx}$, $\epsilon_{0,xy}$, κ_{xx}, κ_{yy}, and κ_{xy}, and hence the linear strain profiles through the thickness of the bonded region. This requires solving the force and moment balance equations in the three directions. Assuming free expansion ($F = 0$ and $M = 0$), the following equations are obtained in xx-direction,

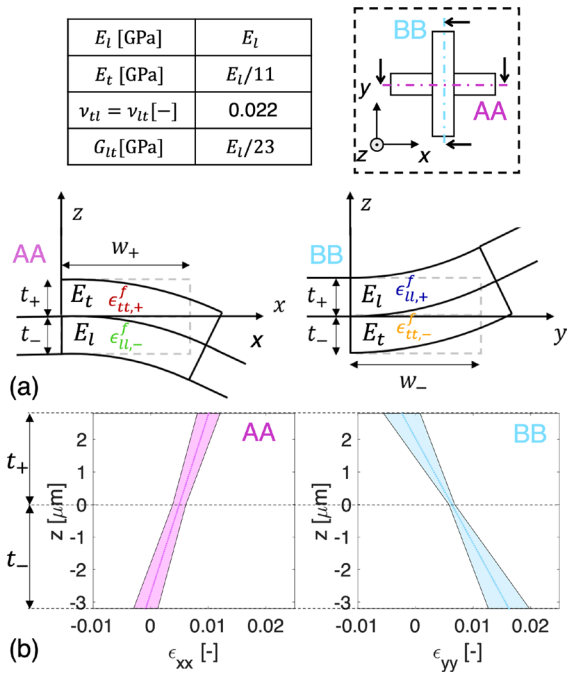

Fig. 7 Bi-layer laminate model used to describe the bending deformation in the bonded area, with **a** the horizontal and vertical cross-section AA and BB of the inter-fiber bond with described bending deformation and the used material parameters, which are obtained from Magnusson and Östlund (2013). The fiber dimensions and hygro-expansion of the freestanding fiber segments (ϵ^f) used in the model are given in, respectively, Tables 1 and 2. **b** The predicted linear strain distributions through the thickness of inter-fiber bond 1 with the confidence area indicating the uncertainty propagation of uncertainties of the input of the model, such as the hygro-expansion and dimensions given in Tables 1 and 2

$$\begin{aligned} F_{xx} &= w_- \int_{t_-}^{0} \sigma_{xx,-} dz + w_- \int_{0}^{t_+} \sigma_{xx,+} dz = 0, \\ M_{xx} &= w_- \int_{t_-}^{0} z\sigma_{xx,-} dz + w_- \int_{0}^{t_+} z\sigma_{xx,+} dz = 0, \end{aligned} \tag{4}$$

in which w_- is the width of the bottom fiber and hence of the bond in xx-direction, and t_- and t_+ the thickness of, respectively, the bottom and top layer forming the laminate. $\sigma_{xx,-}$ and $\sigma_{xx,+}$ are the horizontal stress in, respectively, the bottom and top layer which are related to the strain through the constitutive behavior for orthogonal inter-fiber bonds:

$$\begin{aligned} \sigma_{xx,-} &= C_{11}(\epsilon_{xx} - \epsilon^H_{xx,-}) + C_{12}(\epsilon_{yy} - \epsilon^H_{yy,-}) \\ &\quad + C_{16}(\epsilon_{xy} - \epsilon^H_{xy,-}), \\ \sigma_{xx,+} &= C_{22}(\epsilon_{xx} - \epsilon^H_{xx,+}) + C_{12}(\epsilon_{yy} - \epsilon^H_{yy,+}) \\ &\quad + C_{26}(\epsilon_{xy,+} - \epsilon^H_{xy}). \end{aligned} \tag{5}$$

In which $\epsilon_{xx} = \epsilon_{xx,0} - \kappa_{xx} z$, $\epsilon_{yy} = \epsilon_{yy,0} - \kappa_{yy} z$, and $\epsilon_{xy} = \epsilon_{xy,0} - \kappa_{xy} z$ (Eq. 2), and the stiffness properties (C) for orthogonal bonds are:

$$\begin{aligned} C_{11} &= \frac{E_l}{1 - \nu_{lt}\nu_{tl}}, \quad C_{12} = \frac{\nu_{tl} E_l}{1 - \nu_{lt}\nu_{tl}}, \\ C_{22} &= \frac{E_t}{1 - \nu_{lt}\nu_{tl}}, \quad C_{16} = C_{26} = 0, \quad C_{66} = G_{lt}, \end{aligned} \tag{6}$$

in which E are the relevant Young's moduli and ν the Poisson's ratios. Note that first component of $\sigma_{xx,-}$ in Eq. (5) yields the longitudinal fiber stiffness (C_{11}), while the first component $\sigma_{xx,+}$ yields the transverse fiber stiffness (C_{22}), thereby capturing the orthogonal fiber orientation. The remaining four balance equations for F_{yy}, F_{xy}, M_{yy} and M_{xy} (Eq. 4) along with F_{xx} and M_{xx} are fully formulated in Subsection "Derivation orthogonal inter-fiber bond model" (Supplementary information).

These six balance equations are solved to find the solution for the six unknown quantities ($\epsilon_{xx,0}$, $\epsilon_{yy,0}$, $\epsilon_{xy,0}$, κ_{xx}, κ_{yy}, and κ_{xy}), however, all known quantities must be substituted first. To this end, Table 1 provides the geometries of the top and bottom fiber, i.e. w_-, w_+, t_-, and t_+. The hygroscopic strains (ϵ^H) in each direction are substituted by the corresponding average longitudinal (ϵ^f_{ll}), transverse (ϵ^f_{tt}) or shear strain increase in the freestanding segments (ϵ^f_{lt}) of the top and bottom fiber, which are given in Table 2. Finally, the material properties, i.e. $C_{11}, C_{12}, C_{22}, C_{16}, C_{26}$, and C_{66}, are obtained by substituting the mechanical properties displayed in the table in Fig. 7 into Eq. (6). After substitution, six balance equations (Equation A.1 in the Supplementary information) yielding six unknown quantities ($\epsilon_{xx,0}$, $\epsilon_{yy,0}$, $\epsilon_{xy,0}$, κ_{xx}, κ_{yy}, and κ_{xy}) are attained. Subsequently solving these six balance equations enables finding the solution of the six unknown quantities. Finally, these quantities are substituted into Eq. (2) to find the three equations which describe a linear strain profile through the thickness of the bond, i.e. $\epsilon_{xx}(z) = \epsilon_{xx,0} + \kappa_{xx} z$, $\epsilon_{yy}(z) = \epsilon_{yy,0} + \kappa_{yy} z$, and $\epsilon_{xy}(z) = \epsilon_{xy,0} + \kappa_{xy} z$. The horizontal strain

Table 2 The average longitudinal (ϵ^f_{ll}), transverse (ϵ^f_{tt}) and shear (ϵ^f_{lt}) hygroscopic strains with standard deviation of the freestanding segments of the bottom (−) and top (+) fiber of the tested inter-fiber bonds determined from the wetting slope from 30 to 90% RH and averaged over cycles 2–4

Inter-fiber bond	$\epsilon^f_{ll,-}$ (–)	$\epsilon^f_{tt,-}$ (–)	$\epsilon^f_{lt,-}$ (–)
1	0.0014 ± 0.0006	0.0186 ± 0.0013	− 0.0004 ± 0.0046
2	0.0011 ± 0.0003	0.0245 ± 0.0043	− 0.0016 ± 0.0025
3	0.0017 ± 0.0011	0.0265 ± 0.0021	− 0.0095 ± 0.0061
4	0.0021 ± 0.0016	0.0239 ± 0.0023	− 0.0006 ± 0.0025
Inter-fiber bond	$\epsilon^f_{ll,+}$ (–)	$\epsilon^f_{tt,+}$ (–)	$\epsilon^f_{lt,+}$ (-)
1	0.0011 ± 0.0002	0.0142 ± 0.0023	− 0.0007 ± 0.0007
2	0.0018 ± 0.0002	0.0237 ± 0.0027	− 0.0050 ± 0.0026
3	0.0010 ± 0.0026	0.0370 ± 0.0089	− 0.0041 ± 0.0036
4	0.0013 ± 0.0002	0.0181 ± 0.0024	− 0.0007 ± 0.0012

($\epsilon_{xx}(z)$) and vertical strain ($\epsilon_{yy}(z)$) through the thickness of inter-fiber bond 1 are displayed in Fig. 7b.

The uncertainty in curvature (κ) and interface strain (ϵ_0) are determined by means of propagating the uncertainties of the input parameters of the model, which are the uncertainty in the hygroscopic strain of the freestanding segments considering cycles 2–4 and the fiber dimensional measurement uncertainties. This results in four lines (i.e. $\epsilon_1 = (\epsilon_0 + d\epsilon_0) + (\kappa + d\kappa)z$, $\epsilon_2 = (\epsilon_0 + d\epsilon_0) + (\kappa - d\kappa)z$, $\epsilon_3 = (\epsilon_0 - d\epsilon_0) + (\kappa + d\kappa)z$, and $\epsilon_4 = (\epsilon_0 - d\epsilon_0) - (\kappa - d\kappa)z$), of which the envelope is drawn as a representation of the confidence area in Fig. 7b.

The above-described model is (for now) only applicable to orthogonal inter-fiber bonds, however, bonds 3 and 4 are non-orthogonal (see the bonding angle (α in Table 1)). Hence, the model is adapted to describe the deformation of non-orthogonal inter-fiber bonds, which is described in detail in Subsection "Derivation non-orthogonal inter-fiber bond model" (Supplementary information).

Comparison between bending model and experiments

Since the average strains in the bonded area at the surface of the top fiber ($\epsilon^{BA}_{ll,+}$ and $\epsilon^{BA}_{tt,+}$) and the interface ($\epsilon^{BA}_{ll,-}$ and $\epsilon^{BA}_{tt,-}$) are known from the full-field characterization displayed in Fig. 5, a comparison with the proposed bending model may be conducted for every inter-fiber bond, which is presented in Fig. 8. Moreover, the dashed black line represents the curvature that is determined independently by fitting (with a 2nd order polynomial planar fit) the out-of-plane displacement field resulting from the GDHC analysis of ROI 3a, considering only the central part of the bonded area. This curvature line is plotted starting from the measured strain value at the top surface and adequately matches the experimental data points at the fiber-to-fiber interface for each inter-fiber bond, confirming the reliability of the GDHC analysis. The experimentally and analytically determined curvatures with standard deviation are given in Table 3.

Looking at inter-fiber bonds 1 and 2, the orthogonal inter-fiber bonds, a good match is found between the experimental curvatures ($\kappa^{exp.}$) and those predicted by the laminate model ($\kappa^{mod.}$). The minor mismatches can be attributed to the assumptions made in the model which do not represent the reality, i.e. perfect bonding between the fibers, see Table 1, and no forces and moments acting on the inter-fiber bond. The minor increase at the edges of the bonded area in the $\epsilon_{ll,+}$ curves in Fig. 5 suggests that while the bond is bending upward, the edges of the bonded area are bending downward due to the fixation of the freestanding segments to the sample holder by the nylon wires. This generates an unavoidable moment at the edges of the bonded area resulting in a larger longitudinal strain. Even though the model does not fully comply with reality on these points, a good match between the model and the experiments is obtained, i.e. the experimental strain profiles are within the confidences areas of the model except for inter-fiber bond 3 in horizontal

Table 3 Inter-fiber bond deformation characteristics with the experimentally ($\kappa^{exp.}$) and analytically ($\kappa^{mod.}$) determined curvature in horizontal and vertical directions, and the bond strain predicted by the bi-layer model ($\bar{\epsilon}$) in the horizontal and vertical direction, with or without bending ($\kappa = 0$)

Inter-fiber bond	$\kappa_{xx}^{exp.}$ (m^{-1})	$\kappa_{xx}^{mod.}$ (m^{-1})	$\kappa_{yy}^{exp.}$ (m^{-1})	$\kappa_{yy}^{mod.}$ (m^{-1})	$\bar{\epsilon}_{xx}$ (–)	$\bar{\epsilon}_{yy}$ (–)	$\bar{\epsilon}_{xx}^{\kappa=0}$ (–)	$\bar{\epsilon}_{yy}^{\kappa=0}$ (–)
1	1346 ± 36	1825 ± 298	− 2759 ± 40	− 3101 ± 956	0.0020 ± 0.0012	0.0020 ± 0.0005	0.0026 ± 0.0008	0.0029 ± 0.0007
2	2044 ± 12	2354 ± 111	− 2958 ± 39	− 3562 ± 489	0.0022 ± 0.0013	0.0032 ± 0.0014	0.0029 ± 0.0005	0.0038 ± 0.0004
3	3311 ± 45	1547 ± 520	− 5839 ± 35	− 6790 ± 1126	0.0026 ± 0.0033	0.0023 ± 0.0031	0.0031 ± 0.0017	0.0090 ± 0.0006
4	542 ± 11	908 ± 147	− 4958 ± 39	− 4749 ± 982	0.0032 ± 0.0023	0.0026 ± 0.0017	0.0022 ± 0.0024	0.0057 ± 0.0003

direction. The main reason for this seems to be the significantly lower bonding area compared to the other inter-fiber bonds, as given in Table 1. Finally, the predicted curvature is within 10–20% of the experimental values except for inter-fiber bonds 3 and 4 in horizontal direction.

It can be concluded that the bi-layer laminate model adequately describes the bond mechanics and the strain profiles through the thickness of isolated inter-fiber bonds. Therefore, the next step is to investigate the transmission of the transverse fiber strain in the bonded area for the practically relevant case that the fiber bond is fully confined in a paper fiber network.

Transverse strain transferal in the bonded region

In order to determine the contribution of the transverse fiber strain to the strain at sheet level, it is essential to determine the so-called transverse strain transferal, i.e. the fraction of the transverse strain of one fiber that is transmitted to the bonded fiber in the bonded area. The transverse strain transferal is obtained by first determining the bond strain, predicted by the bi-layer laminate model, in the "longitudinally oriented fiber", i.e. the bottom ($-t_- < z < 0$) and top fiber ($0 < z < t_+$) for, respectively, cross-sections AA and BB, as depicted in Fig. 7. This strain directly contributes to the network, in contrast to the bond strain in the "transversely oriented fiber", i.e. the top ($0 < z < t_+$) and bottom fiber ($-t_- < z < 0$). Because the strain varies linearly through the thickness of the fiber, the horizontal ($\bar{\epsilon}_{xx}$) and vertical bond strain predicted by the bi-layer laminate model ($\bar{\epsilon}_{yy}$) is determined at, respectively $z = -\frac{1}{2}t_-$ and $z = \frac{1}{2}t_+$ with its standard deviation considering cycles 2–4, as given in Table 3. Note that without the bi-layer laminate model, the horizontal bond strain in the bottom fiber could not be determined, because the back of the inter-fiber bond was not captured.

It is generally known from 3D paper characterization using X-ray Computed Tomography that, on average, 50% of the surface of the fibers inside the paper sheet is bonded to neighboring fibers (Borodulina et al. 2016; Urstöger et al. 2020). Therefore, inside a paper sheet, the inter-fiber bonds are much more constrained and consequently much less bending compared to the isolated inter-fiber bonds characterized in the experiments above. Therefore, the earlier computed bond strains do not represent the reality in a paper sheet. Hence, the proposed analytical model, after calibration on the freestanding fiber segments, is adapted to reflect the more realistic zero curvature conditions, i.e. Eq. (2) becomes $\epsilon = \epsilon_0$, resulting in a constant strain through the thickness of the inter-fiber bond. Note that the moment balance (Eq. 4b) becomes irrelevant now and only the force balance (Eq. 4a) needs to be considered. After solving the balance equations, constant bond strain values are found, which are added to Table 3 ($\kappa = 0$). For inter-fiber bonds 1 and 2, consisting of almost equally thick fibers, the bond strain is rather similar in both directions. Whereas for inter-fiber bonds 3 and 4, both consisting of a thicker bottom (horizontal) fiber, the vertical strain is significantly larger, implying that the transverse strain of the bottom fiber can easily stretch the relatively thinner top fiber in its longitudinal direction.

To retrieve the actual transverse strain transferal in, e.g., the horizontal direction, the longitudinal strain of the bottom fiber needs to be subtracted from the horizontal bond strain ($\bar{\epsilon}_{xx}^{\kappa=0}$) given in Table 3, resulting in an additional strain contribution provided by the transverse strain of the top (vertical) fiber. Subsequently dividing the resulting value by the transverse strain of the freestanding part of the top fiber

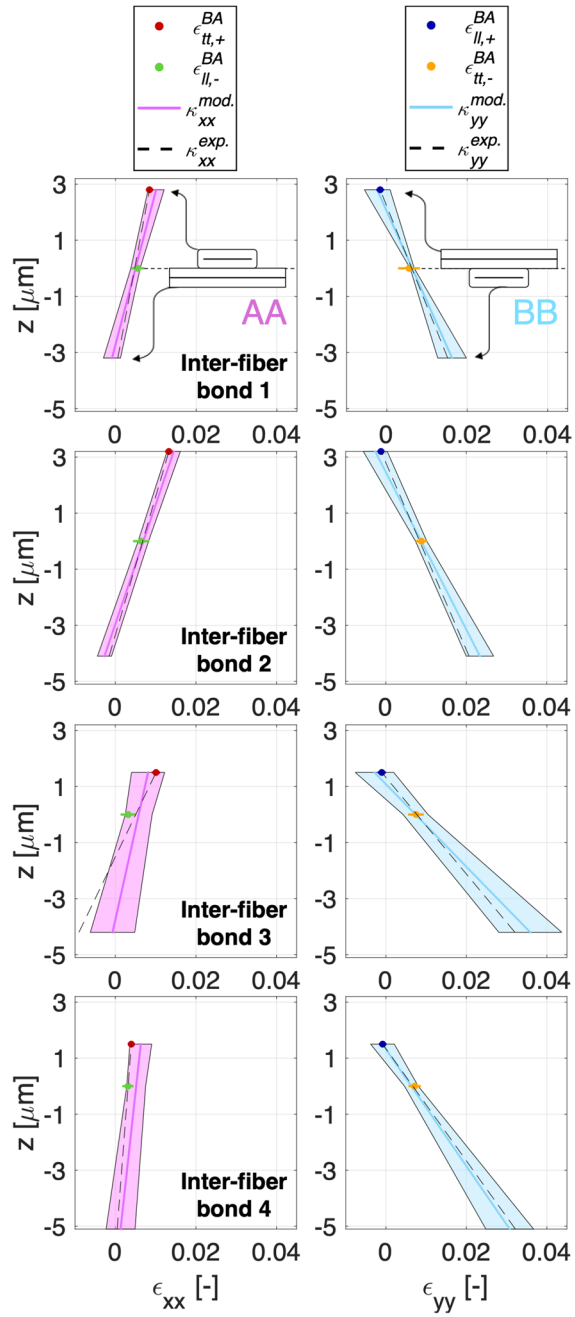

Fig. 8 Comparison between the strain profiles predicted by bi-layer laminate model, based on the strains in the free-standing arms of the fibers, (colored solid lines with uncertainty band) and average bond strains ($\epsilon^{BA}_{ll,+}$, $\epsilon^{BA}_{tt,+}$, $\epsilon^{BA}_{ll,-}$, and $\epsilon^{BA}_{tt,-}$), measured directly at the bonded area on the top surface ($z = t_+$) and the fiber-to-fiber interface ($z = 0$) given in Fig. 5. The curvature of the bonded area (black dashed line) has been independently determined by fitting the GDHC out-of-plane displacement field of ROI 3a, which reveals a good correspondence with the measured bond strains. An adequate match is found between the experimental ($\kappa^{exp.}$) and analytical curvature ($\kappa^{mod.}$) for all inter-fiber bonds, except inter-fiber bond 3, which is explained by the poor bonding area (see Table 1), whereas perfect bonding is assumed in the laminate model

results in a factor (TST_x), representing the fraction of the transverse strain of the top fiber that is transferred to the bottom fiber in the bonded area. The same procedure can be followed for the vertical direction to obtain TST_y, resulting in

$$TST_x = \frac{\bar{\epsilon}^{\kappa=0}_{xx} - \epsilon^{f}_{ll,-}}{\epsilon^{f}_{tt,+}}, \quad \text{and} \quad TST_y = \frac{\bar{\epsilon}^{\kappa=0}_{yy} - \epsilon^{f}_{ll,+}}{\epsilon^{f}_{tt,-}}. \quad (7)$$

The resulting transverse strain transmission factors TST_x and TST_y are listed in Table 4.

Inter-fiber bonds 1 and 2 remarkably show very similar values, both between horizontal and vertical directions, as well as between the two inter-fiber bonds, which can be attributed to similar fiber thickness, the orthogonal inter-fiber bond geometry, and comparable hygroscopic strain given in Tables 1 and 2. The bottom fiber is slightly thicker for both inter-fiber bonds, hence the slightly larger transverse strain transferal in vertical direction. Furthermore, for inter-fiber bonds 3 and 4, the transverse strain transferal in horizontal direction is small, because the bottom fiber is significantly thicker than the top fiber, hence also the large vertical transverse strain transmission. The relatively large standard deviation found for the horizontal transverse strain transferal of inter-fiber bonds 3 and 4 is attributed to the small bond strain (which is almost equal to the longitudinal strain of the bottom fiber) and the relatively large uncertainty on the longitudinal hygro-expansion of the bottom fiber, propagating to a large uncertainty. Additionally, Fig. 5c shows that the longitudinal strain of the bottom fiber is almost equal in the bonded area and the freestanding segments, indicating that the thicker bottom fiber is barely influenced by the thinner top fiber; the same holds for inter-fiber bond 4. In contrast, inter-fiber bonds 1 and 2, consisting of two almost equally thick fibers, show a relatively small uncertainty in the transverse strain transferal factor due to the larger bond strain values.

Reflecting on the work of Nanko and Wu (1995), the authors stated that the transverse strain transferal was not a "100% efficient", whereby it was estimated

Table 4 Transverse stain transferal factor in horizontal and vertical direction, i.e. TST_x and TST_y

Inter-fiber bond	TST_x (–)	TST_y (–)
1	0.085 ± 0.084	0.097 ± 0.051
2	0.076 ± 0.033	0.082 ± 0.027
3	0.038 ± 0.064	0.302 ± 0.202
4	0.006 ± 0.160	0.184 ± 0.034

to be "less than 50%". The findings in this work show that the transferal factor is actually much smaller, i.e. 8.5 ± 4.9% for inter-fiber bonds 1 and 2. The discrepancy can be attributed to the difference in testing methods, i.e. the measurements by Nanko and Wu were limited to (i) two extreme situations, i.e. wet and dry during which the inter-fiber bond morphology (bonded area, degree of wrap around) may significantly change, in contrast to the inter-fiber bonds made prior to testing in this work, of which the geometry remains preserved during testing; (ii) single cycle (from wet to dry) testing during which manufacturing errors affect the outcome, whereas we systematically observe that the first cycle deviates from the subsequent cycles (e.g., Figs. 1 and 6), which motivates the choice in this work to only include the last three out of four cycles, reducing the influence of the dried-in strain due to manufacturing; (iii) measurement of fibers at the paper surface only, not taking into account possible bending effects which may exist, in contrast to inter-fiber bonds that are representative for a location deeper into the paper microstructure as considered here; and (iv) lack of knowledge of the full geometry of the characterized inter-fiber bonds, in contrast to this work. These limitations may also explain the large spread in the bond strain of 1–15% found by Nanko and Wu (1995). In contrast to the work of Nanko and Wu (1995), Brandberg et al. (2020) showed through 3D network modeling that only 4% of the transverse fiber hygro-expansivity contributes to the sheet expansion, implying that the transverse strain transferal is relatively low, similar to the experimental observations presented here. Additionally, future publications (Vonk et al. 2023a, b, c), in which single fibers isolated from prepared handsheets were tested, reveal that the longitudinal fiber hygro-expansion is only slightly lower than the sheet-scale hygro-expansivity, confirming the relatively low contribution of the transverse hygro-expansion to the sheet found in this work and in the network modeling work by Brandberg et al. (2020). Furthermore, the proposed bending and non-bending laminate models predict that *TST* is larger for non-bending than for bending (see Table 3 for inter-fiber bond 1 and 2 which yield almost equal fiber dimensions). It is likely that inter-fiber bonds inside the low porosity paper sheet have less freedom to bend and, consequently, yield a larger *TST* than inter-fiber bonds inside a high porosity paper sheet. This suggests that a larger hygro-expansivity is expected for the low porosity paper sheets. This result complies with literature, which states that low porosity paper sheets exhibit a larger hygro-expansivity, which is commonly attributed to the lower free fiber surface in low porosity paper sheets, which is plausible (Lindner 2018). However, this work reveals that the bending magnitude of inter-fiber bonds can also affect the sheet hygro-expansivity. Finally, the laminate model proposed here can be extended to predict the sheet scale hygro-expansion, for instance by means of the orthogonal network model (Bosco et al. 2015a) consisting of two fibers in which the zero bending laminate model is used to predict the bond strain and a representative porosity is adopted, which is done in Vonk et al. (2023c).

Conclusion

The contribution of the transverse fiber hygro-expansion to the sheet scale has been under debate in the literature for many years. Therefore, in this study, the full-field hygro-expansivity of four isolated inter-fiber bonds was experimentally characterized, allowing identification of the 3D morphological change, transverse strain transferal, and strain gradients in and around the bonded region.

After manufacturing (near) orthogonal inter-fiber bonds, each bond was clamped to a sample holder which allowed imaging of the front and back to determine the fiber thickness and width, degree of wrap around, contact surface and fiber-to-fiber bond angle, which are essential for a proper understanding of the bond hygro-mechanics, as the fiber-to-fiber deviations are rather large. A recently developed Global Digital Height Correlation (GDHC) algorithm dedicated to fiber swelling was extended to determine the full-field hygro-expansion of the inter-fiber bond in and around the bonded area. All inter-fiber bonds revealed

clear bending deformation in the bonded area where the longitudinal direction of one fiber is attached to the transverse direction of the other fiber, which is driven by the significantly larger transverse compared to longitudinal hygro-expansivity of the (orthogonally) bonded fibers. Furthermore, the GDHC results showed a transverse strain decrease near the bonded area, which is attributed to the low longitudinal hygro-expansion of the bonded fiber. As the top fiber covers the bottom fiber in the bonded region, the strain field at the fiber-to-fiber interface surface is unknown, but needed for understanding the bond (hygro-)mechanics. Therefore, interpolation of the strain field to the left and right of the bonded area was employed to determine the strain field at the interface, revealing an increased longitudinal strain of the bottom fiber, which is attributed to the large transverse strain of the top fiber that stretches the bottom fiber in its longitudinal direction. Finally, all inter-fiber bonds showed similar deformations, highlighting the accuracy of the method and the reproducibility of the inter-fiber bond (hygro-)mechanics, even for bonds consisting of significantly deviating fiber dimensions and fiber-to-fiber bond angles.

An analytical bi-layer laminate model was used to describe the bending deformation in the bonded region. This model requires material parameters, dimensions, and the hygro-expansion of free segments of the fibers constituting the bond, all measured in the experiments or known from the literature. This model allows to predict the strain profile in horizontal and vertical direction through the thickness of the bonded area. Because the average bond strain in both directions at two locations through the thickness, i.e., the top fiber surface and the fiber-to-fiber interface surface, of the inter-fiber bond are known from the full-field characterization, a comparison was conducted and an adequate match was found. Moreover, the curvatures predicted by the model are also in good agreement with those obtained directly by fitting the out-of-plane displacement field from GDHC. Hence, the laminate model can predict the bond (hygro-)mechanics well. Different boundary conditions applied to the laminate model allowed to predict the transverse strain transferal, i.e. the fraction of the transverse strain of one fiber stretching the bonded fiber in its longitudinal direction which contributes to the sheet scale hygro-expansion. It was found that, for two inter-fiber bonds of similar fiber dimensions, the transverse strain transferal is relatively weak, which is in close agreement with recent findings from 3D network modeling (Brandberg et al. 2020), and deviates from suggestions made in earlier inter-fiber bond work by Nanko and Wu (1995).

Acknowledgments The authors would like to acknowledge Marc van Maris of Eindhoven University of Technology for lab support. Also, the authors would like to acknowledge Louis Saes and Thomas Anijs of Canon Production Printing for extensive technical discussions and suggestions.

Author Contributions NV: Conceptualization, Methodology, Software, Validation, Investigation, Writing—original draft, Visualization. RP: Methodology, Supervision, Funding acquisition, Writing—review & editing. MG: Methodology, Resources, Writing—review & editing, Supervision, Funding acquisition. JH: Conceptualization, Methodology, Validation, Resources, Writing—review & editing, Supervision, Funding acquisition.

Funding This work is part of an Industrial Partnership Programme (i43-FIP) of the Foundation for Fundamental Research on Matter (FOM), which is part of the Netherlands Organization for Scientific Research (NWO). This research programme is co-financed by Canon Production Printing, University of Twente, Eindhoven University of Technology.

Data Availibility The presented data will be made available on request.

Declarations

Conflict of interest The authors declare that they have no known competing financial interests or personal relationships that could have appeared to influence the work reported in this work.

Ethical approval This article does not contain any studies with human participants or animals performed by any of the authors.

Consent of publication The authors hereby consent to publication of the present research work in this journal, if selected for publication.

References

Alava M, Niskanen KJ (2006) The physics of paper. Rep Prog Phys 69:669. https://doi.org/10.1088/0034-4885/69/3/R03

Berglund LA (2011) 12. Wood biocomposites—extending the property range of paper products. In: Mechanics of paper

products. De Gruyter, pp 231–254. https://doi.org/10.1515/9783110254631.231
Borodulina S, Kulachenko A, Wernersson ELG, Hendriks CLL (2016) Extracting fiber and network connectivity data using microtomography images of paper. Nordic Pulp Pap Res J 31:469–478. https://doi.org/10.3183/npprj-2016-31-03-p469-478
Bosco E, Peerlings RHJ, Geers MGD (2015a) Explaining irreversible hygroscopic strains in paper: a multi-scale modelling study on the role of fibre activation and micro-compressions. Mech Mater 91:76–94. https://doi.org/10.1016/j.mechmat.2015.07.009
Bosco E, Peerlings RHJ, Geers MGD (2015b) Predicting hygro-elastic properties of paper sheets based on an idealized model of the underlying fibrous network. Int J Solids Struct 56:43–52. https://doi.org/10.1016/j.ijsolstr.2014.12.006
Bosco E, Peerlings RHJ, Geers MGD (2016) Local network effects on hygroscopic expansion in digital ink-jet printing. Nordic Pulp Pap Res J 31:684–691. https://doi.org/10.3183/npprj-2016-31-04-p684-691
Bosco E, Peerlings RHJ, Geers MGD (2017) Asymptotic homogenization of hygro-thermo-mechanical properties of fibrous networks. Int J Solids Struct 115:180–189. https://doi.org/10.1016/j.ijsolstr.2017.03.015
Bosco E, Peerlings RHJ, Lomans BAG, van der Sman CG, Geers MGD (2018) On the role of moisture in triggering out-of-plane displacement in paper: from the network level to the macroscopic scale. Int J Solids Struct 154:66–77. https://doi.org/10.1016/j.ijsolstr.2017.04.005
Brandberg A, Motamedian HR, Kulachenko A, Hirn U (2020) The role of the fiber and the bond in the hygroexpansion and curl of thin freely dried paper sheets. Int J Solids Struct 193:302–313. https://doi.org/10.1016/j.ijsolstr.2020.02.033
Czibula C, Brandberg A, Cordill MJ, Matković A, Glushko O, Czibula C, Kulachenko A, Teichert C, Hirn U (2021) The transverse and longitudinal elastic constants of pulp fibers in paper sheets. Sci Rep 11:1–13. https://doi.org/10.1038/s41598-021-01515-9
Fellers C (2007) The interaction of paper with water vapour, vol 2. Walter de Gruyter, Berlin
Fischer WJ, Hirn U, Bauer W, Schennach R (2012) Testing of individual fiber-fiber joints under biaxial load and simultaneous analysis of deformation. Nordic Pulp Pap Res J 27:237–244. https://doi.org/10.3183/npprj-2012-27-02-p237-244
Forsström J, Torgnysdotter A, Wågberg L (2005) Influence of fibre/fibre joint strength and fibre flexibility on the strength of papers from unbleached kraft fibres. Nordic Pulp Pap Res J 20:186–191. https://doi.org/10.3183/npprj-2005-20-02-p186-191
Gilli E, Kappel L, Hirn U, Schennach R (2009) An optical model for polarization microscopy analysis of pulp fibre-to-fibre bonds. Compos Interfaces 16:901–922. https://doi.org/10.1163/092764409X12477474036798
Hirn U, Schennach R (2015) Comprehensive analysis of individual pulp fiber bonds quantifies the mechanisms of fiber bonding in paper. Sci Rep 5:1–9. https://doi.org/10.1038/srep10503
Hoefnagels JPM, van Dam K, Vonk NH, Jacobs L (2022) Accurate strain field measurement during strip rolling by exploiting recurring material motion with time-integrated digital image correlation. Exp Mech 62:603–625. https://doi.org/10.1007/s11340-021-00781-y
Jajcinovic M, Fischer WJ, Hirn U, Bauer W (2016) Strength of individual hardwood fibres and fibre to fibre joints. Cellulose 23:2049–2060. https://doi.org/10.1007/s10570-016-0895-0
Jajcinovic M, Fischer WJ, Mautner A, Bauer W, Hirn U (2018) Influence of relative humidity on the strength of hardwood and softwood pulp fibres and fibre to fibre joints. Cellulose 25:2681–2690. https://doi.org/10.1007/s10570-018-1720-8
Kappel L, Hirn U, Bauer W, Schennach R (2009) A novel method for the determination of bonded area of individual fiber-fiber bonds. Nordic Pulp Pap Res J 24:199–205. https://doi.org/10.3183/npprj-2009-24-02-p199-205
Kappel L, Hirn U, Bauer W, Gilli E, Schennach R (2010a) Revisiting polarized light microscopy for fiber-fiber bond area measurement—part II: proving the applicability. Nordic Pulp Pap Res J 25:71–75. https://doi.org/10.3183/npprj-2010-25-01-p071-075
Kappel L, Hirn U, Gilli E, Austria W, Schennach R (2010b) Revisiting polarized light microscopy for fiber-fiber bond area measurement—part I: theoretical fundamentals. Nordic Pulp Pap Res J 25:65–70. https://doi.org/10.3183/npprj-2010-25-01-p065-070
Kulachenko A (2021) Moisture-induced deformations. Mech Pap Prod. https://doi.org/10.1515/9783110619386-009
Kulachenko A, Gradin P, Uesaka T (2005) Tension wrinkling and fluting in heatset web offset printing process. Post buckling analyses. In: 13th Fundamental research symposium on advances in paper science and technology location: Univ Cambridge, Cambridge, ENGLAND Date: SEP, 2005, The Pulp and Paper Fundamental Research Society, pp 1075–1099
Larsson PA, Wågberg L (2008) Influence of fibre–fibre joint properties on the dimensional stability of paper. Cellulose 15:515–525. https://doi.org/10.1007/s10570-008-9203-y
Lindner M (2018) Factors affecting the hygroexpansion of paper. J Mater Sci 53:1–26. https://doi.org/10.1007/s10853-017-1358-1
Magnusson MS, Östlund S (2013) Numerical evaluation of interfibre joint strength measurements in terms of three-dimensional resultant forces and moments. Cellulose 20:1691–1710. https://doi.org/10.1007/s10570-013-9939-x
Maraghechi S, Bosco E, Suiker ASJ, Hoefnagels JPM (2023) Experimental characterisation of the local mechanical behaviour of cellulose fibres: an in-situ micro-profilometry approach. Cellulose. https://doi.org/10.1007/s10570-023-05151-6
Motamedian HR, Kulachenko A (2019) Simulating the hygroexpansion of paper using a 3d beam network model and

concurrent multiscale approach. Int J Solids Struct 161:23–41. https://doi.org/10.1016/j.ijsolstr.2018.11.006
Nanko H, Ohsawa J (1989) Mechanisms of fibre bond formation. Fundam Papermak 2:783–830
Nanko H, Wu J (1995) Mechanisms of paper shrinkage during drying. International paper physics conference. Niagara-on-the-Lake, Canada, pp 103–113
Neggers J, Hoefnagels JPM, Hild F, Roux S, Geers MGD (2014) Direct stress-strain measurements from bulged membranes using topography image correlation. Exp Mech 54:717–727. https://doi.org/10.1007/s11340-013-9832-4
Neggers J, Blaysat B, Hoefnagels JPM, Geers MGD (2016) On image gradients in digital image correlation. Int J Numer Methods Eng 105:243–260. https://doi.org/10.1002/nme.4971
Niskanen KJ, Kuskowski SJ, Bronkhotst CA (1997) Dynamic hygroexpansion of paperboards. Nordic Pulp Pap Res J 12:103–110. https://doi.org/10.3183/npprj-1997-12-02-p103-110
Page DH, Tydeman PA (1962) A new theory of the shrinkage, structure and properties of paper. In: The formation and structure of paper, vol 1, pp 397–425
Page DH, Tydeman PA, Hunt M (1962) The formation and structure of paper. Technical Section British Paper & Board Makers' Association, London, p 397
Pister KS, Dong SB (1959) Elastic bending of layered plates. J Eng Mech Div 85:1–10. https://doi.org/10.1061/JMCEA3.0000100
Reissner E, Stavsky Y (1961) Bending and stretching of certain types of heterogeneous aeolotropic elastic plates. J Appl Mech 28:402–408. https://doi.org/10.1115/1.3641719
Samantray P, Peerlings RHJ, Bosco E, Geers MGD, Massart TJ, Rokoš O (2020) Level set-based extended finite element modeling of the response of fibrous networks under hygroscopic swelling. J Appl Mech. https://doi.org/10.1115/1.4047573
Schmied FJ, Teichert C, Kappel L, Hirn U, Schennach R (2012) Joint strength measurements of individual fiber-fiber bonds: an atomic force microscopy based method. Rev Sci Instrum 83:073902. https://doi.org/10.1063/1.4731010
Schmied FJ, Teichert C, Kappel L, Hirn U, Bauer W, Schennach R (2013) What holds paper together: nanometre scale exploration of bonding between paper fibres. Sci Rep 3:1–6. https://doi.org/10.1038/srep02432
Sellén C, Isaksson P (2014) A mechanical model for dimensional instability in moisture-sensitive fiber networks. J Compos Mater 48:277–289. https://doi.org/10.1177/0021998312470576
Shafqat S, Hoefnagels JPM (2021) Cool, dry, nano-scale DIC patterning of delicate, heterogeneous, non-planar specimens by micro-mist nebulization. Exp Mech 61:917–937. https://doi.org/10.1007/s11340-020-00686-2
Shafqat S, Van der Sluis O, Geers MGD, Hoefnagels JPM (2018) A bulge test based methodology for characterizing ultra-thin buckled membranes. Thin Solid Films 660:88–100. https://doi.org/10.1016/j.tsf.2018.04.005
Sormunen T, Ketola A, Miettinen A, Parkkonen J, Retulainen E (2019) X-ray nanotomography of individual pulp fibre bonds reveals the effect of wall thickness on contact area. Sci Rep 9:1–7. https://doi.org/10.1038/s41598-018-37380-2
Stratton RA, Colson NL (1990) Dependence of fiber/fiber bonding on some papermaking variables. MRS Online Proceedings Library (OPL) 197. https://doi.org/10.1557/PROC-197-173
Strömbro J, Gudmundson P (2008) Mechano-sorptive creep under compressive loading—a micromechanical model. Int J Solids Struct 45:2420–2450. https://doi.org/10.1016/j.ijsolstr.2007.12.002
Uesaka T (1994) General formula for hygroexpansion of paper. J Mater Sci 29:2373–2377. https://doi.org/10.1007/BF00363429
Uesaka T, Qi D (1994) Hygroexpansivity of paper: effects of fibre-to-fibre bonding. J Pulp Pap Sci 20:J175–J179
Urstöger G, Kulachenko A, Schennach R, Hirn U (2020) Microstructure and mechanical properties of free and restrained dried paper: a comprehensive investigation. Cellulose 27:8567–8583. https://doi.org/10.1007/s10570-020-03367-4
Vonk NH, Verschuur NAM, Peerlings RHJ, Geers MGD, Hoefnagels JPM (2020) Robust and precise identification of the hygro-expansion of single fibers: a full-field fiber topography correlation approach. Cellulose 27:6777–6792. https://doi.org/10.1007/s10570-020-03180-z
Vonk NH, Geers MGD, Hoefnagels JPM (2021) Full-field hygro-expansion characterization of single softwood and hardwood pulp fibers. Nordic Pulp Pap Res J 36:61–74. https://doi.org/10.1515/npprj-2020-0071
Vonk NH, Peerlings RHJ, Geers MGD, Hoefnagels JPM (2023a) Effect of restrained versus free drying on hygro- expansion of hardwood and softwood fibers and paper handsheet. Cellulose 30:11135–11156. https://doi.org/10.1007/s10570-023-05473-5
Vonk NH, Peerlings RHJ, Geers MGD, Hoefnagels JPM (2023b) Re-understanding the in-plane hygroexpansion of freely and restrained dried paper handsheets. Adv Pulp Paper Res 2022(1):421–440
Vonk NH, van Spreuwel WPC, Anijs T, Peerlings RHJ, Geers MGD, Hoefnagels JPM (2023c) Transient hygro-and hydro-expansion of freely and restrained dried paper: the fiber-network coupling. arXiv preprint arXiv:2303.15480
Wahlström T (2009) Development of paper properties during drying, vol 2. Walter de Gruyter, Berlin